MICROROBOTS

Multifunctional surface microrollers for targeted cargo delivery in physiological blood flow

Yunus Alapan[1]*, Ugur Bozuyuk[1]*, Pelin Erkoc[1,2], Alp Can Karacakol[1,3], Metin Sitti[1,4†]

Mobile microrobots offer great promise for minimally invasive targeted medical theranostic applications at hard-to-access regions inside the human body. The circulatory system represents the ideal route for navigation; however, blood flow impairs propulsion of microrobots especially for the ones with overall sizes less than 10 micrometers. Moreover, cell- and tissue-specific targeting is required for efficient recognition of disease sites and long-term preservation of microrobots under dynamic flow conditions. Here, we report cell-sized multifunctional surface microrollers with ~3.0 and ~7.8-micrometer diameters, inspired by leukocytes in the circulatory system, for targeted drug delivery into specific cells and controlled navigation inside blood flow. The leukocyte-inspired spherical microrollers are composed of magnetically responsive Janus microparticles functionalized with targeting antibodies against cancer cells (anti-HER2) and light-cleavable cancer drug molecules (doxorubicin). Magnetic propulsion and steering of the microrollers resulted in translational motion speeds up to 600 micrometers per second, around 76 body lengths per second. Targeting cancer cells among a heterogeneous cell population was demonstrated by active propulsion and steering of the microrollers over the cell monolayers. The multifunctional microrollers were propelled against physiologically relevant blood flow (up to 2.5 dynes per square centimeter) on planar and endothelialized microchannels. Furthermore, the microrollers generated sufficient upstream propulsion to locomote on inclined three-dimensional surfaces in physiologically relevant blood flow. The multifunctional microroller platform described here presents a bioinspired approach toward in vivo controlled propulsion, navigation, and targeted active cargo delivery in the circulatory system.

INTRODUCTION

Mobile microrobots powered by biological or synthetic motors are promising candidates for the next generation of theranostic (e.g., targeted active cargo delivery) and micromanipulation applications in the human body because of their active propulsion and steerability (*1*–*3*). Although the medical microrobotics field has advanced over the past decade with considerable improvements in fabrication (*4*, *5*), propulsion (*6*–*8*), and imaging (*9*, *10*), their applications inside the human body have been mainly limited to superficial tissues (e.g., inside the eye), locations with relatively easier access routes (e.g., the gastrointestinal tract and peritoneal cavity), and stagnant or low-velocity fluidic environments. Minimally invasive administration and deployment of medical microrobots to tissues in deeper locations inside the human body with substantial fluidic flows (e.g., the circulatory/vascular system) remains a grand challenge toward their future high-impact in vivo medical applications.

The circulatory system is the natural fluidic transport network of the body, reaching all organs and the deepest tissues (*11*). Even though the circulatory system represents the ideal route for accessing the target disease locations, harsh physical conditions (e.g., blood flow, densely crowded heterogeneous fluidic environment) within the vessels impair the motion of microrobots, especially the ones with sizes less than 10 μm (*12*). On the other hand, surface motion of leukocytes, the only motile cells in the bloodstream, on vessel walls is enabled by their margination to the vessel wall (*13*), a cell-free layer (*14*), and decreased flow velocities compared with the vessel center (*15*). Therefore, vessel wall–enabled surface motion of leukocytes can be mimicked in surface-crawling or -rolling microrobots for efficient propulsion in blood flow (*16*).

Another unique aspect of leukocytes is their recruitment toward damaged or infected tissues with high spatiotemporal resolution (*17*, *18*). Site-specific recruitment of leukocytes is enabled by recognition of specific ligands (e.g., selectins) on endothelial cells by recognition moieties (e.g., P-selectin glycoprotein ligand-1) present on leukocytes (*15*, *17*). Similar strategies for biorecognition of target cells (e.g., activated endothelial cells and cancer cells) are highly desired for autonomous operation of microrobots, especially in the absence of high-resolution medical imaging modalities (*3*). Such recognition moieties could also enable binding and tethering of microrobots to the target cells or tissues, which is crucial for their long-term preservation and operation at the target tissue under dynamic flow conditions.

Here, we report leukocyte-inspired multifunctional microrollers, at the size scale of blood cells, for targeted active cargo delivery and locomotion under blood flow. The microrollers (3.0 and 7.8 μm in diameter) were composed of spherical Janus microparticles with a magnetically responsive half-side and a silica half-side for biochemical functionalities and cargo loading (Fig. 1A). Targeted cargo delivery was realized by surface-functionalized cell-specific antibodies and light-cleavable anticancer drug molecules [doxorubicin (DOX)]. The multifunctional microrollers were actuated and steered by external rotating magnetic fields, reaching up to a translational speed of 600 μm/s, corresponding to 76 body lengths per second (BLPS). Cell-targeting capability was tested by specific binding of microrollers to cancer cells within a heterogeneous cell population during active rolling locomotion. Furthermore, the multifunctional microrollers were also capable of upstream (against-flow) locomotion and controlled navigation on planar and endothelialized surfaces in physiologically relevant blood flow (up to 2.5 dyn/cm^2). The microrollers were also able to locomote against blood flow at physiologically

---

[1] Physical Intelligence Department, Max Planck Institute for Intelligent Systems, 70569 Stuttgart, Germany. [2] Faculty of Engineering and Natural Sciences, Bahcesehir University, Istanbul 34353, Turkey. [3] Department of Mechanical Engineering, Carnegie Mellon University, Pittsburgh, PA 15213, USA. [4] School of Medicine and School of Engineering, Koç University, Istanbul 34450, Turkey.
*These authors contributed equally to this work and share first authorship.
†Corresponding author. Email: sitti@is.mpg.de

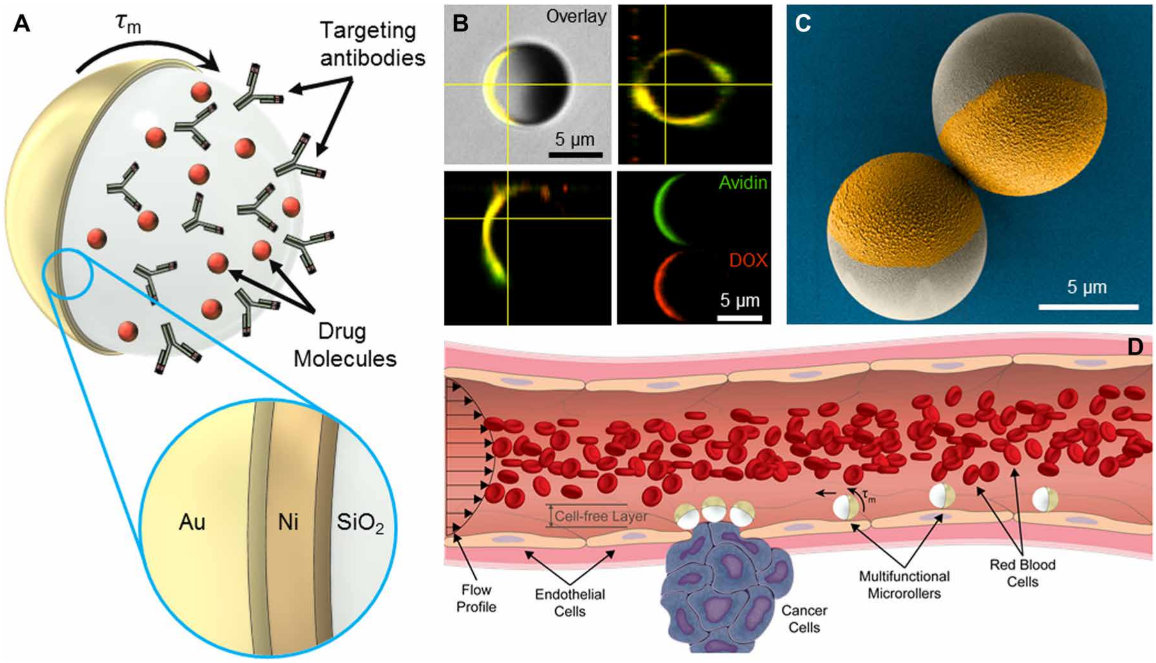

Fig. 1. Multifunctional microrollers for targeted active cargo delivery in blood flow. (**A**) Magnetically actuated Janus microrollers consist of a silica core and nickel/gold (Ni/Au) half caps. The silica side is functionalized with targeting antibodies and drug molecules. τ_m represents the magnetic torque acting on the particle. (**B**) Confocal microscopy image of a typical microroller (7.8 μm) showing functionalized streptavidin, for antibody binding, and drug molecules (DOX). (**C**) Pseudo-colored scanning electron microscopy image of the fabricated microrollers. (**D**) Conceptual schematic depicting magnetically actuated microrollers locomoting against blood flow (upstream) on the vessel wall. Multifunctional microrollers can selectively recognize target cells (e.g., cancer cells) via cell-specific antibodies, enabling autonomous targeting capability.

relevant conditions on inclined three-dimensional (3D) surfaces. The multifunctional microroller design provided here establishes the proof of concept for microrobot surface propulsion in blood flow and could inspire new directions for their navigation in the circulatory system.

RESULTS

Multifunctional microrollers were designed to have a magnetically responsive Ni/Au nanofilm-sputtered half-side and a silica half-side decorated with DOX molecules and antibodies for targeting specific cell types (Fig. 1, A and B). Metallic nanolayers of the microrollers were fabricated by sequential sputtering of Ni and Au (Fig. 1C and fig. S1), where the Au layer prevents oxidation of the Ni layer and ensures biocompatibility. Upon application of vertical rotating magnetic fields, Janus microparticles would roll on nearby surfaces and translate linearly, where steering is achieved by changing the orientation of the rotating magnetic field. We hypothesize that, similar to leukocytes migrating in blood vessels, the multifunctional microrollers would be able to locomote on cell monolayers and in dynamic blood flow conditions (Fig. 1D). Furthermore, multifunctional microrollers could recognize target cells via cell-specific antibodies functionalized on their surfaces (Fig. 1D).

Functionalization of drug molecules and targeting antibodies on the silica half-side of the microrollers was realized by grafting amino groups on the surface using 3-aminopropyltrimethoxysilane (APTES) (Fig. 2A). Biotinylated *N*-hydroxysuccinimide (NHS) was conjugated to amino groups, which enabled the binding of biotin-conjugated human epidermal growth factor receptor 2 (HER2) antibodies (anti-HER2) through biotin-avidin-biotin coupling (Fig. 2A). Biotin-avidin coupling is one of the strongest noncovalent interaction in nature (*19*) and used to ensure robustness of the targeting capabilities in harsh physical conditions, such as under high-shear flow conditions or high-frequency rolling. On the other hand, DOX molecules were functionalized on the same side through a photocleavable *o*-nitrobenzyl linker, which allows on-demand light-triggered release (*20*). Whereas *o*-nitrobenzyl linker binds to the amino groups through the NHS end, azide-modified DOX is conjugated to the alkyne end via copper(I)-catalyzed click chemistry [copper-catalyzed azide-alkyne cycloaddition (CuAAC)] (Fig. 2A). Confocal microscopy images of Janus microrollers confirmed silica-side selective functionalization of DOX and avidin (Fig. 1B and fig. S2). The loading capacities of microrollers were characterized by incubating different microroller concentrations (1×10^6, 4×10^6, and 8.5×10^6 microrollers/ml) in the same amount of DOX and streptavidin, resulting in initial loading concentrations of 6, 12.5, and 50 nmol DOX/10^6 particles and 6, 12.5, and 50 μg streptavidin/10^6 particles. The average loaded DOX amounts were similar irrespective of the initial DOX amount (fig. S3), which might be due to the steric hindrance effect of the linear linker and DOX molecules (*21*). On the other hand, the loaded streptavidin amount increased with increased amounts of initial streptavidin (fig. S3). The highest loading conditions (50 nmol DOX/10^6 particles and 50 μg streptavidin/10^6 particles) were used for the rest of the study.

After fabrication and functionalization of the microrollers, we tested their targeting and light-triggered drug release capability in vitro. To test the targeting, we added bare and anti-HER2–functionalized microrollers on HER2-expressing SKBR3 breast cancer cells (fig. S4).

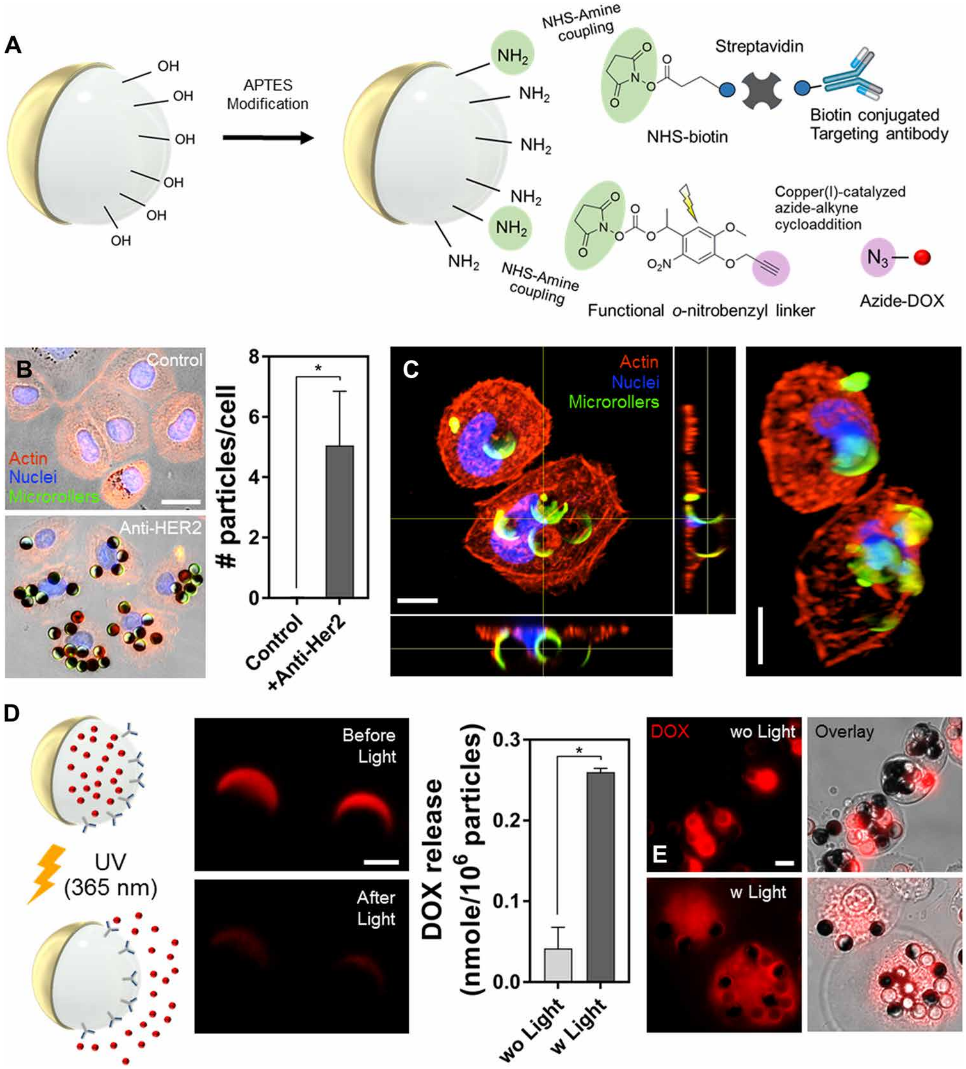

Fig. 2. Targeted binding and light-triggered drug release from multifunctional microrollers. (**A**) Chemical functionalization of targeting antibodies and light-cleavable drug molecules on the Janus microrollers. Amino groups are grafted on the silica side using APTES modification. Light-cleavable DOX are bound to the silica side through a functional *o*-nitrobenzyl linker, whereas the targeting antibodies (anti-HER2) are conjugated through biotin-avidin-biotin interactions. (**B**) Microrollers with functionalized targeting antibodies (anti-HER2) were bound to HER2-expressing breast cancer cells (SKBR3), whereas bare microrollers were washed away. Scale bar, 25 μm. Number of bound microrollers with antibody functionalization was significantly greater than bare microrollers (Student's *t* test, $P < 0.05$). Error bars represent the SD of the mean. (**C**) Confocal microscopy images show binding of the Janus microrollers to breast cancer cells from their silica sides. Scale bars, 10 μm. (**D**) Light-triggered drug release from microrollers was achieved by exposure to 365-nm UV light. Fluorescence signals from DOX molecules on microrollers were diminished after light exposure for 30 s. Scale bar, 5 μm. Microrollers showed burst release of DOX (~0.25 nmol/10^6 particles) after light exposure (Student's *t* test, $P < 0.05$). Error bars represent the SD of the mean. (**E**) Drug delivery into HER2-expressing SKBR3 cells was achieved by targeted binding of DOX-loaded microrollers and light-triggered release. Fluorescence microscopy images show DOX signal within the cells 1 day after light exposure, whereas DOX signal was confined to the microrollers without light exposure.

Microrollers with HER2 antibodies were bound to the SKBR3 cells (5 ± 1.8 particles per cell), whereas the bare particles were flushed away completely (Fig. 2B and fig. S5). Here, introducing microrollers incubated in (for 30 min) and administered with whole blood had no effect on their targeting capability (fig. S5C). Confocal microscopy images further confirmed binding of microrollers to the cells from their antibody-functionalized silica side (Fig. 2C and fig. S6). For light-triggered drug release, we used 365-nm ultraviolet (UV) light for photocleaving the linker and releasing the DOX molecules (Fig. 2D). After 30 s of light exposure (44 mW/cm^2), fluorescence signal of the microrollers was diminished (Fig. 2D). The microrollers showed burst release characteristics upon light exposure with ~0.25 nmol/10^6 particles DOX release, whereas there was no release without UV exposure (Fig. 2D). We further tested targeted drug delivery potential by treating SKBR3 cells with DOX and anti-HER2–functionalized microrollers. After targeted binding to SKBR3 cells, light exposure resulted in depleted fluorescence in the microrollers, whereas the DOX signal was strongly detected within the cells (Fig. 2E). On the other hand, without the light exposure, the DOX signal was confined to the microrollers (Fig. 2E).

Before demonstrating the multifunctionality of the microrollers during active motion, we first characterized their surface locomotion behavior and performance (Fig. 3). Motion of the microrollers directly depends on the applied magnetic field strength and the magnetic properties of the particles. The microrollers were premagnetized toward their metallic cap under a uniform 1.8-T magnetic field (fig. S7, A and B) and retained their magnetization direction under external fields up to 20 mT (fig. S7, C and D; see note S1 for details). The magnetic microrollers followed the external uniform rotating magnetic fields, resulting in microroller rotation (fig. S8 and movie S1). The presence of a hydrodynamic nearby boundary creates a mismatch of hydrodynamic mobility between the top and bottom of the microparticle, which enables translation of magnetic torque into linear motion (*22*–*24*) (Figs. S9 to S12; see note S1 for details). Direction of the microroller motion was controlled by changing the orientation of the rotating magnetic field (Fig. 3A and movie S1). Microroller translational speed depends almost linearly on the applied magnetic field frequency until a critical threshold (step-out frequency) is reached, after which the particle rotation speed is no longer linearly proportional to the field rotation frequency (Fig. 3B). The increased Ni film thickness resulted in higher step-out frequencies and, thus, higher speeds. Speeds of microrollers with 480- to 2000-nm Ni film thicknesses reached up to 600 μm/s, corresponding

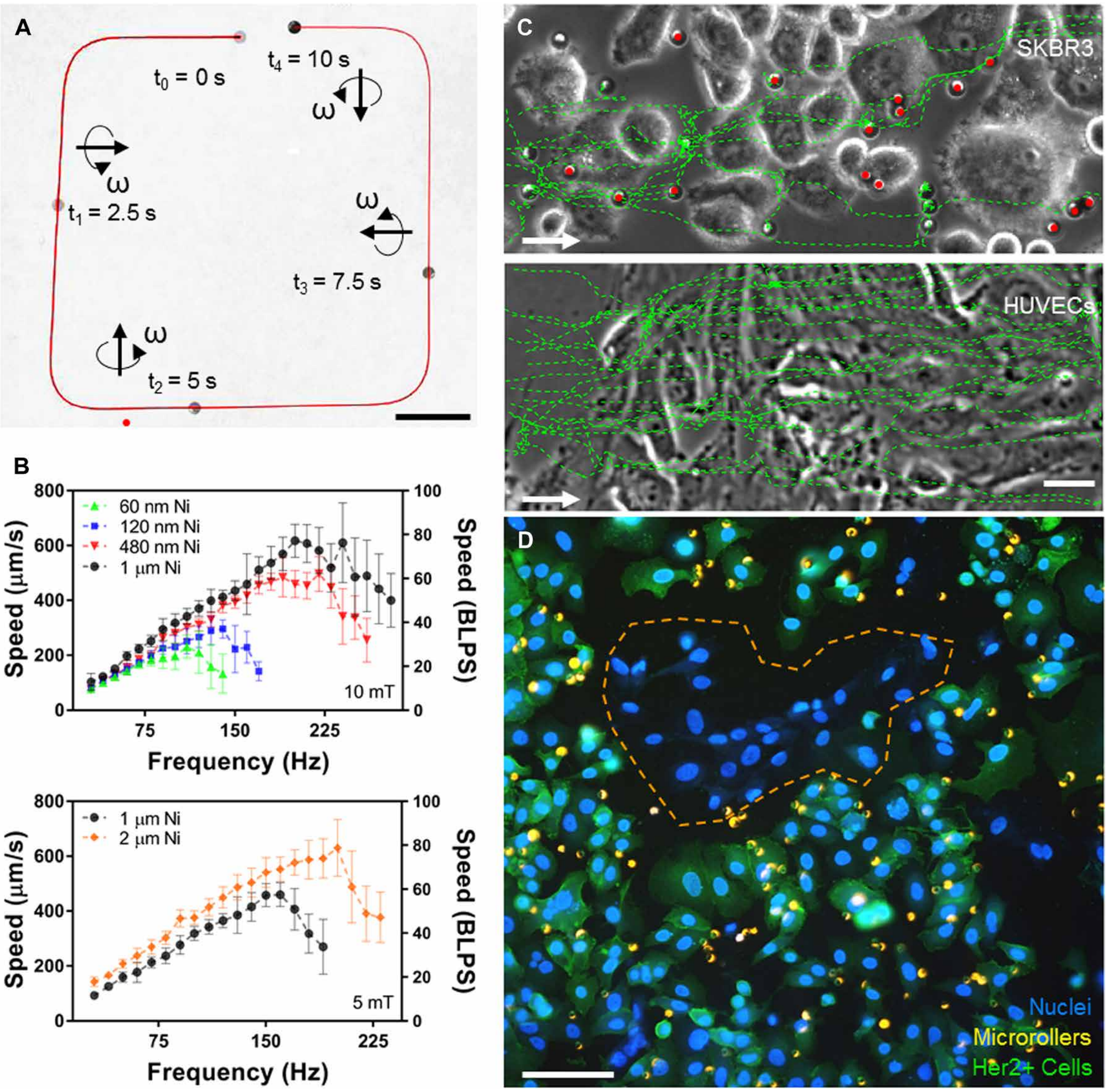

Fig. 3. Selective targeting of cancer cells by magnetically actuated microrollers. (**A**) A single microroller translating on a nearby surface via surface-enabled rolling under rotating magnetic fields. Trajectory of the microroller was controlled by changing the direction of the field rotation axis (50 Hz, 10 mT). Scale bar, 50 μm. (**B**) Average speeds of microrollers with different Ni film thicknesses. Speed of microrollers with 480- to 2000-nm Ni film thicknesses could reach up to 600 μm/s, corresponding to 76 BLPS. Error bars represent the SD of the mean. (**C**) Microrollers with HER2 antibody selectively bind to SKBR3 cells during active rolling, whereas they freely pass over HUVECs. The dashed green lines show the trajectories of microrollers passed over the cells, and the red dots indicate the microrollers bound to the target cells. White arrows indicate the direction of microroller motion. Scale bar, 25 μm. (**D**) HER2 antibody–functionalized microrollers were selectively bound to HER2-expressing SKBR3 cancer cells, but not to HUVECs, during active rolling in a coculture environment. Dashed orange lines mark the area of HUVECs without HER2 expression. HER2 expression and Janus microrollers are indicated by green and yellow fluorescence signals, respectively. Scale bar, 100 μm.

to a speed of 76 BLPS at around ~200 to 220 Hz, which is the limit of the magnetic actuation setup used in this study (Fig. 3B and movie S1).

Next, we investigated active targeting of cancer cells by mobile microrollers. During active rolling, while moving on cell monolayers, microrollers with HER2 antibodies bound to SKBR3 cells. However, on the endothelial cells [human umbilical vein endothelial cells (HUVECs)], the microrollers traveled freely without any interaction (Fig. 3C and movie S2). Selective targeting of the microrollers was further evidenced by propelling and steering over a heterogeneous cell layer composed of SKBR3 cells and HUVECs. Microrollers functionalized with HER2 antibodies were only bound to the HER2-expressing SKBR3 cancer cells within the mixed cell monolayer, whereas the normal HUVECs were completely free of microrollers (Fig. 3D). These results show the autonomous cell recognition capability of the mobile microrollers enabled by surface-functionalized targeting moieties.

Any microrobot administered into the bloodstream should be able to not only steer along the blood flow but also locomote upstream for controlled navigation and targeting. In blood vessels, walls represent the most advantageous location for locomotion, as evident in leukocyte migration, because of the decreased blood flow velocity. To demonstrate the locomotion of the microrollers under flow conditions, we first tested their upstream motion capability in phosphate-buffered saline (PBS) within microfluidic channels mimicking physiologically relevant wall shear stress values (0.9 to 1.2 dyn/cm^2) of the postcapillary venules and veins (*25–27*). Without any applied magnetic torque, the microrollers were drifted along the flow direction, and, upon application of a rotating magnetic field, the microrollers could locomote against the flow (Fig. 4A and movie S3). Analyses of drifting speed, when there was no magnetic field, and upstream rolling speed (at 120 Hz) of microrollers with 480-nm-thick Ni films at different wall shear stresses showed a decrease in upstream propulsion speed with increasing wall shear stresses (Fig. 4B). At 1.2 dyn/cm^2, upstream propulsion speeds of microrollers with 2-μm Ni film thickness (169.7.5 ± 40.0 μm/s) were 3.5 times greater than the speed of microrollers with 480-nm-thick Ni films (46.5 ± 44.2 μm/s) (Fig. 4C). These results indicate that additional fluidic drag on the microrollers results in reduced step-out frequencies. At the same shear stress, the microrollers with 2-μm Ni film thickness reached their top speed (422.2 ± 51.2 μm/s) when the actuation frequency was increased to 180 Hz (Fig. 4D). To further test the locomotion capability of the microrollers on endothelial cells and under physiological flow conditions, we developed a branching microfluidic system (75-μm channel height) (Fig. 4, E and F). The microrollers actuated at 180 Hz were able to locomote within the endothelialized channels in a controlled manner under PBS flow at 1.2 dyn/cm^2 (Fig. 4G and movie S3).

To test the propulsion of the microrollers in more realistic conditions, we used fresh whole blood (mouse CD1 whole blood). The microrollers were propelled and navigated with ease inside the whole blood without any flow (static) (fig. S13 and movie S4). We further tested their locomotion against whole blood flow and showed that the microrollers were able to locomote upstream when actuated at 120 Hz for 1.2 dyn/cm^2 wall shear stress (Fig. 5A and movie S4). The average propulsion speeds against the blood flow at 1.2 dyn/cm^2 were 55.5 ± 20.8 μm/s and 156.7 ± 36.6 μm/s for microrollers with 480-nm and 2-μm Ni film thicknesses, respectively, at 120 Hz (Fig. 5B). We further tested the upper threshold of wall shear stress that the microrollers can locomote against. The microrollers with 2-μm Ni film thickness were able to generate sufficient propulsion force to locomote at 2.5 dyn/cm^2 while barely maintaining their position and slowly drifting in the flow direction at 4 dyn/cm^2 (Fig. 5C, fig. S14, and movie S4). Other than upstream locomotion capability, controlled motion in all directions is also crucial for precise navigation in blood flow. Although trajectory of a microroller was almost linear when actuated upstream, cross-stream actuation resulted in diagonal trajectories that were a combination of the actuation and flow directions (Fig. 5D and movie S4). To further highlight the active controlled navigation capability, we locomoted and steered the microrollers in bifurcating blood flow (Fig. 5E). Under continuous blood flow (1.2 dyn/cm^2), two microrollers were navigated from the left branch to the right branch and then back to the left branch again by performing upstream, cross-migration, and downstream locomotion behaviors (Fig. 5E, fig. S15, and movie S4).

Another potential challenge for the translation of the microrollers is the 3D nature of the vascular system. The microroller platform presented in our work takes advantage of the nearby boundaries for propulsion. Therefore, the boundaries guide the locomotion of the microrollers. When rolled on a curved or inclined surface, there is an extra gravitational force acting on the microroller. However, at the size scale of our microrollers, the

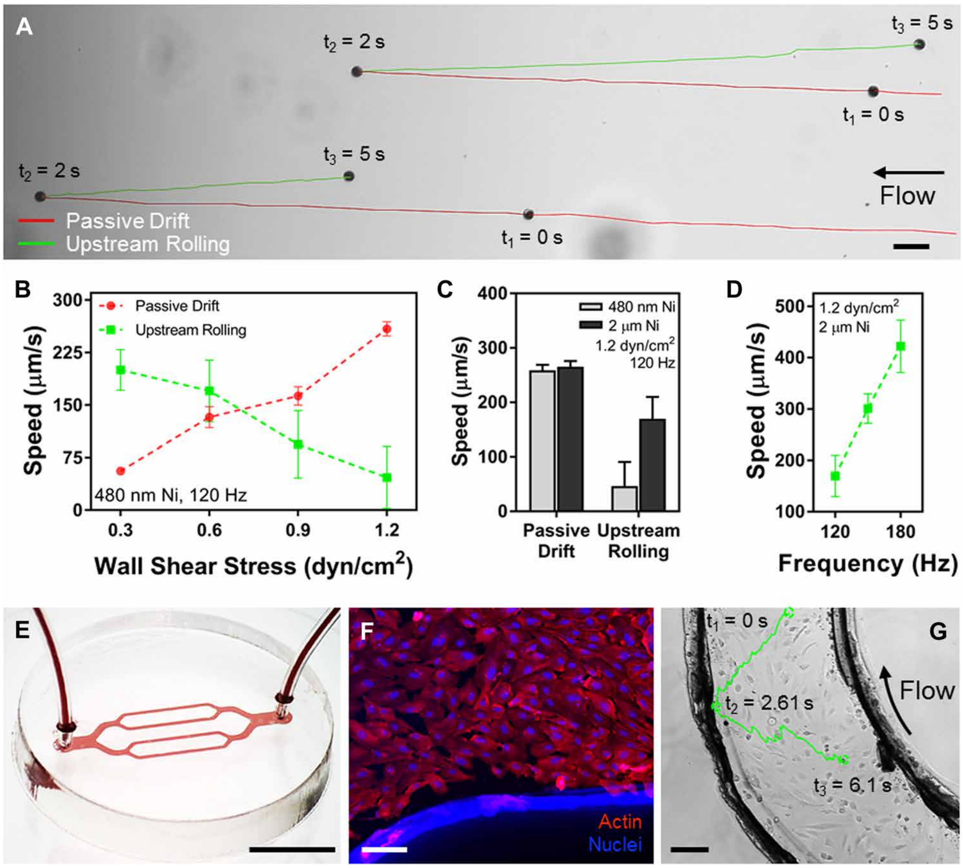

Fig. 4. Active upstream propulsion of multifunctional microrollers in physiologically relevant PBS flow. (**A**) Time-lapse images of microrollers with 480-nm Ni thickness, first drifting in the flow direction (red line, until $t_2 = 2$ s) and then actively rolling (under 180 Hz, 10 mT) against the flow (green line, until $t_3 = 5$ s) at physiological wall shear stress (1.2 dyn/cm^2). Scale bar, 25 μm. (**B**) Average drift and upstream rolling speeds of microrollers with 480-nm Ni thickness depending on different wall shear stress values. Error bars represent the SD of the mean. (**C**) Average drift and upstream rolling speeds of microrollers with 480-nm and 2-μm Ni thicknesses actuated at 120 Hz in PBS flow at 1.2 dyn/cm^2. Error bars represent the SD of the mean. (**D**) Frequency-dependent upstream propulsion speed of microrollers with 2-μm Ni thickness in PBS flow at 1.2 dyn/cm^2. Error bars represent the SD of the mean. (**E**) An endothelialized microfluidic system with branched channels. Scale bar, 5 mm. (**F**) Fluorescent microscopy images showing the nuclei and actin fibers of HUVECs cultured inside the microfluidic system. Scale bar, 100 μm. (**G**) Upstream propulsion of a microroller on endothelialized channels in PBS flow at 1.2 dyn/cm^2. Scale bar, 100 μm.

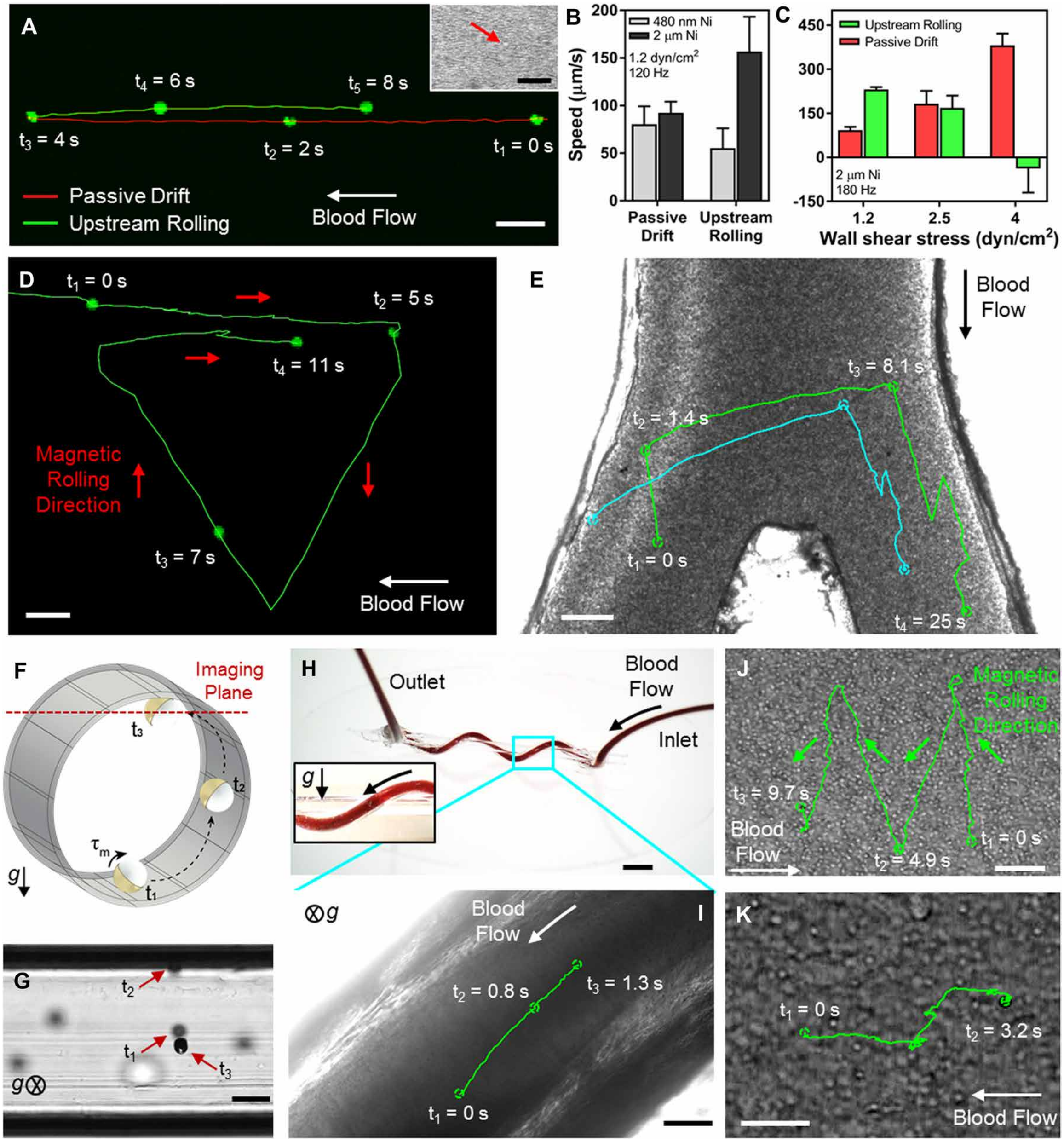

Fig. 5. Active propulsion of multifunctional microrollers against blood flow in flat and 3D surfaces. (**A**) Time-lapse fluorescence images of a microroller (480-nm Ni thickness), first drifting in the direction of blood flow (red line, until $t_3 = 4$ s) and then rolling upstream in blood flow upon magnetic actuation (green line, until $t_5 = 8$ s). Scale bar, 25 µm. Inset shows the bright-field image of the microroller actuated in blood flow. The red arrow indicates the microroller. Scale bar, 50 µm. (**B**) Average drift and upstream rolling speed of microrollers with 480-nm and 2-µm Ni thickness (actuated at 120 Hz) in blood flow (1.2 dyn/cm^2). Error bars represent the SD of the mean. (**C**) Average drift and upstream rolling speed of microrollers with 2-µm Ni thickness (actuated at 180 Hz) in blood flow (1.2 to 4 dyn/cm^2). Error bars represent the SD of the mean. (**D**) Controlled triangle trajectory of a single microroller in blood flow. Scale bar, 25 µm. (**E**) Active navigation of microrollers in bifurcating blood flow. Microrollers propelled upstream from the left branch to the right side and then locomoted downstream in blood flow. Solid lines indicate microroller trajectories. Scale bar, 100 µm. (**F** to **I**) Locomotion of microrollers in 3D surfaces in static conditions and under blood flow. (F and G) A microroller actuated in a cylindrical tube (200 Hz) climbs through the curved wall and reaches the top of the tube. Scale bar, 25 µm. *g* indicates the gravity direction. (H and I) Upstream propulsion of a microroller (actuated at 180 Hz) in physiologically relevant blood flow conditions (1.2 dyn/cm^2) in a 3D microfluidic system composed of a tubing coiled around a glass capillary. Inset shows the inclination of the channel from the front side. Scale bars, 2 mm (H) and 100 µm (I). *g* indicates the gravity direction. (**J**) Controlled triangle trajectory of a single 3-µm microroller in blood flow. Scale bar, 50 µm. (**K**) Upstream propulsion of a 3-µm microroller on endothelialized channels in blood flow at 1.2 dyn/cm^2. Scale bar, 20 µm.

propulsion force generated by the microroller, when actuated at high frequencies, dominates the gravitational force, enabling the motion of the microrollers at inclined surfaces as well (Figs. S16 to S18; see note S2 for the inclined wall analysis). To demonstrate locomotion on inclined surfaces, we introduced the microrollers into a cylindrical tube with an inner diameter of 125 µm. When actuated toward the wall, the microroller could climb toward the top of the tube by following the curved boundaries against the gravity (Fig. 5, F and G, and movie S5). To further test the locomotion capability of the microrollers on inclined surfaces under physiological blood flow, we built a 3D microfluidic system composed of a tubing coiled around a glass capillary (Fig. 5H). When actuated (180 Hz) in the upstream direction, the microrollers were able to locomote against the blood flow (1.2 dyn/cm^2) with ease, reaching an average speed of 119.6 ± 21.6 μm/s (Fig. 5I and movie S5).

The size of the microrollers presented here is in the same scale with blood cells. Nevertheless, they are at the upper limit of capillaries and may cause blockage because of their rigidity. Therefore, scaling down the size of the microrollers without losing their propulsion capabilities could be crucial for real-world applications. To test the propulsion capability of microrollers at smaller scales, we fabricated microrollers out of 3-μm silica particles half-coated with a 1-μm Ni film. Step-out frequency of the microrollers was on par with their larger counterparts in terms of BLPS (fig. S19A). Although the small microrollers were not able to withstand PBS flow at 1.2 dyn/cm^2 when actuated at 120 Hz, their average upstream propulsion speed was 52 μm/s at 180 Hz (fig. S19B). The small microrollers were also able to locomote against and navigate freely in blood flow at 1.2 dyn/cm^2 on flat (Fig. 5J; Fig. S19, C and D; and movie S6) and endothelialized surfaces (Fig. 5K and movie S6).

DISCUSSION

The circulatory system appears to be the obvious route for deployment and navigation of medical microrobots given its access to all organs and distant tissues (*28*). Even though magnetic pulling of large-scale magnetic particles (>1 mm) in large vessels has been demonstrated (*29*, *30*), dynamic flow conditions severely impair the propulsion of swimming microrobots with much smaller sizes (*31*) down to single-cell scale. Considering the decreased flow velocities and a cell-free layer near the vessel walls, surface-enabled propulsion (e.g., rolling or crawling) of microrobots would be more efficient and robust than swimming (*32*) despite the popular vision of swimming microrobots in blood flow at the vessel cross-section center (*33*). The only motile cells in the blood flow (leukocytes) can actively migrate at the walls of the venules by taking advantage of the wall distance–dependent effects described above (*14*, *15*). In this study, we describe a leukocyte-inspired biomimetic strategy taking advantage of the same effects for active propulsion against flow direction. The multifunctional magnetic microrollers described here enable controlled navigation in complex blood flow configurations at physiological wall shear stresses.

The proposed microrollers could reach propulsion speeds up to 600 μm/s, representing one of the fastest magnetic microrobots in the literature at its given size scale to the best of our knowledge. Along with the microrobot performance, upstream propulsion capability of the microrollers also depends on the applied flow rate, thus the fluidic forces on the microrollers. In the body, physiological shear stress on vessel walls varies widely depending on the vessel type, from 0.76 to 7.6 dyn/cm^2 in veins to 11.4 to 30.4 dyn/cm^2 in large arteries (*25*). Here, we showed upstream propulsion and controlled navigation of the microrollers under wall shear stresses up to 2.5 dyn/cm^2, corresponding to the physiological levels in postcapillary and small venules (*27*, *34*, *35*), which are the main sites for leukocyte extravasation as well (*15*). The main limitation for the speed of microrollers in static and against flow conditions in this study was the maximum frequency (~200 to 220 Hz) that could be applied with our current magnetic actuation setup. Upstream propulsion at higher wall shear stresses can be achieved by applying higher frequencies. Although we showed upstream locomotion of the microrollers on 3D surfaces against gravity, continuous locomotion on surfaces with an inclination greater than 90° and upside locomotion would require additional forces, such as magnetic (*36*) or acoustic (*16*), perpendicular to the near wall. In addition, upstream propulsion of the microrollers on topographically heterogeneous surfaces, such as cell layers, requires a detailed investigation because the motion of the microrollers was not monolithic in contrast to the motion on flat surfaces.

Autonomous recognition of target cells within a heterogeneous cell population is another crucial feature for targeted theranostic applications of mobile microrobots, especially in the absence of functional real-time imaging modalities. For applications targeting cells within heterogeneous populations or sporadic events over a large area, autonomous biorecognition of disease sites is essential for efficient therapeutic delivery (*37*, *38*). Here, we showed that cell-specific targeting can be achieved by functionalization of antibodies against specific cells on the microroller surface. The microroller design presented here directly aims for recognition of target cells through receptors available on the membrane surface because the micrometer size of our particles would prevent their fast internalization in contrast to nanoparticles. Although we have used HER2 antibodies for targeting HER2-expressing breast cancer cells here, this approach can be expanded for targeting other cancer types or vascular diseases using different targeting moieties. Furthermore, attachment/binding of microrobots to the target cells via targeting moieties could enable their long-term preservation at the target site, which could be especially crucial in dynamic environments, such as in blood flow environments.

Preservation of therapeutic cargo within the microrobot's body until reaching the target site is crucial for maximizing the therapeutic effect. Diffusion-based cargo delivery in microrobotic systems may suffer from the burst release of cargo molecules before reaching the target site. Stimuli-responsive release systems have been widely used to enable on-demand release of therapeutic cargo from micro-/nanoparticles (*39*). In this study, we used light-cleavable linkers for on-demand release of DOX molecules upon targeting specific cells. Although the low tissue penetration depth and cell viability issues at longer exposure times are limiting factors for UV-triggered release systems (*40*), recent advances in optical upconversion processes (e.g., conversion of near-infrared light to UV light) could enable their deeper and more feasible applications (*41*). Furthermore, other stimuli-responsive release mechanisms—including pH, temperature (i.e., hyperthermia through the metallic nanofilm layer on the microroller using remote electromagnetic waves), and ultrasound—could also be integrated into the microroller platform described here.

The microroller design presented here allows facile and high-throughput fabrication along with bioactive surfaces for integration of versatile functionalities, including cell-specific targeting, cargo loading, and stimuli-responsive cargo release. The multifunctional microrollers reported here demonstrate the proof of concept for upstream propulsion and controlled navigation of microrobots in physiologically relevant blood flow conditions. The capabilities of surface-rolling magnetic microrobots introduced in this work represent a unique multifunctionality with propulsion speeds that can reach up to 600 μm/s (76 BLPS), upstream propulsion and controlled navigation in physiologically relevant blood flow in 3D channels, and cell-specific targeting within a heterogeneous population during active motion. The design approach provided here establishes the groundwork for development of next-generation microrobots for controlled navigation and cargo delivery in the circulatory system.

MATERIALS AND METHODS

Fabrication of magnetic microrollers

Magnetically actuated, spherical Janus microrollers were fabricated by sequentially sputtering Ni (60- to 2-μm-thick) and Au (20-nm-thick) nanofilms on a predried monolayer of silica (SiO_2) particles of 7.8- and 3-μm diameters (microParticles GmbH) using a benchtop sputter coating system (Leica EM ACE600, Leica Microsystems). After sputtering, magnetization direction of the Janus microparticles was oriented toward out of the cap by applying a 1.8-T uniform magnetic field in a vibrating-sample magnetometer (MicroSense, Lowell, MA). Ni and Au nanofilm-sputtered microparticles were then released from the substrate via sonication in ethanol. Scanning electron microscopy imaging of the Janus microparticles was performed via a Zeiss Ultra 550 Gemini scanning electron microscope (Carl Zeiss Inc., Oberkochen, Germany).

Functionalization of DOX and anti-HER2 on microrollers

The silica sides of the microrollers were modified with targeting antibodies (anti-HER2) and light-cleavable drug molecules (DOX) through amino groups on the surface. APTES was used to graft amino groups to the silica side (*42*). Briefly, 50 μl of APTES was added to 1 ml of ethanol solution containing Janus microrollers in a concentration of 4×10^6 microrollers/ml. The mixture was vortexed for 3 hours, followed by incubation at 65°C for 1 hour. The particles were centrifuged and washed five times with ethanol. Then, the particles were dispersed in PBS (1×) for further steps.

A functional *o*-nitrobenzyl photocleavable linker [1-(5-methoxy-2-nitro-4-prop-2-ynyloxyphenyl)ethyl *N*-succinimidyl carbonate, LifeTein LLC, Somerset, NJ)] was conjugated to the amino end of the microrollers by NHS-amino coupling chemistry. Briefly, the particles were dispersed in the linker solution [5 mM in anhydrous dimethyl sulfoxide (DMSO)], and the mixture was vortexed for 3 hours. The particles were then washed two times with DMSO and resuspended in the PBS. After this step, azide-modified doxorubicin (Azide-DOX, LifeTein LLC, Somerset, NJ) was conjugated to the alkyne end of the linker molecule through CuAAC, which is a simple and convenient tool for conjugation of biomolecules under mild conditions (*43*). The microparticles were vortexed in a solution containing 50 μM azide-modified DOX, 100 μM $CuSO_4$, 5 mM sodium ascorbate, and 500 μM tris(3-hydroxypropyltriazolylmethyl)amine for 3 hours. The particles were then washed twice with DMSO and PBS to remove any remaining free residues.

ErbB2 (HER-2) monoclonal antibody (Thermo Fisher Scientific, Waltham, MA) was also conjugated to the silica side of the Janus particles via biotin-streptavidin-biotin interaction (*44*). First, residual amino groups of the microrollers were modified with biotin by incubating the microparticles in NHS-biotin (EZ-Link NHS-Biotin, Thermo Fisher Scientific, Waltham, MA) solution (5 mg/ml in DMSO) for 3 hours. After washing with DMSO and PBS, the microparticles were treated with fluorescently labeled streptavidin (Alexa Fluor 488 and 532, 50 μg/ml in PBS, Thermo Fisher Scientific, Waltham, MA) for 1 hour and then washed twice with PBS. Next, the microrollers were incubated with biotin-conjugated HER-2 antibodies for 1 hour and washed twice with PBS to remove nonbound remnants. Then, the microrollers were treated with bovine serum albumin solution (3% w/v in PBS) to prevent nonspecific attachment of the microrollers. The microrollers were finally resuspended in PBS for further experiments. For all demonstrations, both DOX and anti-HER2 were functionalized on the microroller surfaces, except the control group in Fig. 2B. To prepare bare (unmodified) microrollers, we treated APTES-modified microrollers with 3% (w/v) albumin solution. To test the loading capacity, we incubated different concentrations of Janus microrollers (1×10^6, 4×10^6, and 8.5×10^6 microrollers/ml) in the same amount of linker-DOX and streptavidin. To calculate the loaded amount of DOX and streptavidin, we centrifuged the microrollers, and we measured the fluorescence of the supernatants using a plate reader (BioTek Gen5 Synergy 2, Bad Friedrichshall). Loading amounts were calculated using DOX and fluorescently labeled streptavidin (Alexa Fluor 488) calibration curves.

Drug release and targeting cancer cells

SKBR3 cells (HTB-30, American Type Culture Collection, Manassas, VA) were grown in Dulbecco's modified Eagle's medium supplemented with 10% v/v fetal bovine serum and 1% v/v penicillin-streptomycin (Gibco, Grand Island, NY, USA) at 37°C in a 5% CO_2, 95% air humidified atmosphere. After growing to confluence, cells were reseeded into μ-Slide 8-well plates (Ibidi GmbH, Gräfelfing, Germany) at a density of 25×10^3 cells per well and incubated for 2 days. For testing the microroller binding to the target cells, 1×10^6 microrollers (with and without HER-2 antibody) were added into wells and incubated for 10 min. Then, the wells were flushed with fresh media, washed twice with PBS, and fixed with formaldehyde (4% in PBS) for 10 min. The cells were then stained with Alexa Fluor 647 Phalloidin and Hoechst 33342 (Thermo Fisher Scientific, Waltham, MA) for actin filament and nucleus fluorescent visualization, respectively. For visualization of HER2 expression, cells in the control wells were incubated with HER-2 monoclonal antibodies conjugated with Alexa Fluor 488 (Thermo Fisher Scientific, Waltham, MA). Fluorescent and bright-field microscopy imaging was performed with a Nikon (Eclipse, Ti-E) inverted motorized microscope (Nikon Corp., Tokyo, Japan), and numbers of bound particles on SKBR3 cells were counted manually from six images (with an area of 0.145 mm^2 each). Confocal microscopy imaging of the microrollers bound to the SKBR3 cells was performed with a Nikon Ti-E spinning disk confocal microscope (Nikon Corp., Tokyo, Japan).

For quantitative characterization of light-triggered drug release, 1×10^6 microrollers functionalized with light-cleavable DOX were dispersed in 1 ml of PBS and irradiated under UV light (44 mW/cm^2) for 30 s. The particles were then centrifuged, and fluorescence of the supernatant was measured using a plate reader (BioTek Gen5 Synergy 2, Bad Friedrichshall). Amount of released DOX from microrollers was determined using a DOX calibration curve. To realize triggered drug release into cells, 1×10^6 microrollers functionalized with HER-2 antibodies and light-cleavable DOX were added onto SKBR3 cells, incubated for 10 min, and irradiated under UV light (365 nm) for 30 s. After 1 day, DOX fluorescence intensities of the particles and the cells were recorded.

Selective targeting of cancer cells by mobile microrollers

The magnetic microrollers were actuated and steered using a custom-made five-coil electromagnetic setup (fig. S20). The coil setup was placed on an inverted optical microscope (Zeiss Axio Observer A1, Carl Zeiss, Oberkochen, Germany). Each coil was controlled independently by a current controller (Escon 70/10, Maxon Motor AG), and current values were determined by precalculated field-to-current ratios. Step-out frequency of microrollers of 60- to 2-μm-thick Ni nanofilm on a glass substrate immersed in PBS was determined under constant 10-mT rotating magnetic fields by gradually increasing the frequency up to 300 Hz. The mean speeds of the microrollers were determined using an in-house MATLAB code for video processing, which performs object detection and tracking.

For selective targeting of cancer cells, HUVECs were used as controls and grown in EBM-2 Basal Medium (CC-3156, Lonza) supplemented with EGM-2 SingleQuots (CC-4176, Lonza) in a 5% CO_2, 95% air humidified atmosphere. SKBR3 cells and HUVECs (Lonza, Basel, Switzerland) were seeded either separately or together into custom-made wells. Microrollers were added to wells with either SKBR3 cells or HUVECs or their coculture and actuated to translate on cell monolayers. Cells in the coculture well were then fixed with formaldehyde (4% in PBS) and stained for nucleus (Hoechst) and HER2 expression (anti-HER2 Alexa Fluor 488) for fluorescent detection of microrollers bound to the SKBR3 cells compared with the HUVECs.

Active controlled locomotion in blood flow

Flow experiments were performed in a closed microchannel (75 μm height by 3 mm width by 12 mm length) composed of a poly(methyl methacrylate) (PMMA) top piece encompassing fluidic connections, a double-sided tape defining the channel shape and height, and a glass bottom piece (*45*). The fluidic connections in the PMMA top piece and the desired channel shape in the double-sided tape were micromachined using a CO_2 laser cutting system (Epilog Laser, Scottsdale, AZ). For the bifurcating and endothelialized microfluidic channels, double-sided adhesive tape was micromachined using a UV laser system (LPKF ProtoLaser U3, Garbsen, Germany). HUVECs were introduced into the microchannels coated with fibronectin (0.1 mg/ml for 1 hour at room temperature) at a concentration of 10^7 cell/ml and cultured with media flow at 1.2 dyn/cm^2 for 24 hours. For the 3D microfluidic system, tubing (Silastic, Cole-Parmer, Wertheim, Germany), with an inner and outer diameter of 0.3 and 0.6 mm, respectively, was coiled around a glass capillary (0.6 mm outer diameter).

The microrollers, mixed with PBS or whole blood (mouse CD1 whole blood, Innovative Research Inc., Peary Court), were loaded into syringes and injected into the microfluidic channels at controlled flow rates (5 to 20 μl/min for PBS and 1.12 to 12.26 μl/min for whole blood) using a syringe pump (KD Scientific Inc., Holliston, MA). Desired flow rate was adjusted to generate wall shear stresses in the range of physiological values. Wall shear stress values were calculated according to

$$\tau = \frac{6\eta Q}{wh^2} \tag{1}$$

where h and w are the channel height and width, respectively, η is the dynamic fluid viscosity, and Q is the volumetric flow rate.

Statistical analysis

All quantitative values were presented as means ± SD of the mean. Student's t test was used for the statistical analysis, and statistical significance was set at 95% confidence level for all tests ($P < 0.05$).

SUPPLEMENTARY MATERIALS

robotics.sciencemag.org/cgi/content/full/5/42/eaba5726/DC1

Note S1. The basic principle of rolling
Note S2. Inclined wall analysis
Fig. S1. Fabrication steps of the Janus microrollers.
Fig. S2. Confocal microscopy images of streptavidin-functionalized (green, top image) and DOX-functionalized (red, bottom image) microrollers with 3D reconstruction of the z-stack planes.
Fig. S3. Loading amount of DOX and streptavidin onto Janus microrollers.
Fig. S4. HER2 expression on SKBR3 breast cancer cells and HUVECs.
Fig. S5. Binding of bare and anti-HER2 modified microrollers to cancer cells.
Fig. S6. Confocal microscopy images showing the Janus microrollers attached to the breast cancer cells with 3D reconstruction of the z-stack planes.
Fig. S7. Magnetic properties of the sputtered Ni films.
Fig. S8. Magnetic rotation of a Janus microroller under an applied uniform rotating magnetic field.
Fig. S9. Rolling propulsion mechanism.
Fig. S10. The force balance on a rolling sphere rotating near a wall.
Fig. S11. Theoretical and experimental speeds of microrollers.
Fig. S12. Effect of density on separation distance and translational velocity according to the theoretical calculations for $f = 100$ Hz.
Fig. S13. Active locomotion and controlled steering of a microroller in whole blood under static conditions (120 Hz rolling frequency).
Fig. S14. Upstream rolling of microrollers in blood flow.
Fig. S15. Navigation snapshots in bifurcating blood flow conditions.
Fig. S16. The force balance on a rolling sphere on an inclined wall.
Fig. S17. The relation between $F_P/F_G\sin\theta$ with respect to rolling frequency and wall angle.
Fig. S18. Percent decrease in translational velocity (U) relative to the translational velocity on a flat wall with respect to rolling frequency and wall angle.
Fig. S19. Propulsion of microrollers made out of 3-μm silica particles in flow.
Fig. S20. Photo of the magnetic field generation setup composed of five electromagnetic coils placed on an inverted optical microscope.
Table S1. Parameters used in the theoretical calculations.
Movie S1. Magnetic actuation and control of Janus microrollers.
Movie S2. Selective binding of multifunctional microrollers to cancer cells.
Movie S3. Propulsion of the microrollers in physiologically relevant flow conditions in PBS.
Movie S4. Upstream propulsion and controlled navigation in physiologically relevant blood flow.
Movie S5. Locomotion of microrollers on 3D surfaces.
Movie S6. Navigation of 3-μm-sized microrollers in blood flow.
References (*46*–*48*)

REFERENCES AND NOTES

1. M. Sitti, *Mobile Microrobotics* (MIT Press, 2017).
2. P. Erkoc, I. C. Yasa, H. Ceylan, O. Yasa, Y. Alapan, M. Sitti, Mobile microrobots for active therapeutic delivery. *Adv. Ther.* **2**, 1800064 (2019).
3. Y. Alapan, O. Yasa, B. Yigit, I. C. Yasa, P. Erkoc, M. Sitti, Microrobotics and microorganisms: Biohybrid autonomous cellular robots. *Annu. Rev. Control Robot. Auton. Syst.* **2**, 205–230 (2019).
4. Y. Alapan, B. Yigit, O. Beker, A. F. Demirörs, M. Sitti, Shape-encoded dynamic assembly of mobile micromachines. *Nat. Mater.* **18**, 1244–1251 (2019).
5. J. Cui, T.-Y. Huang, Z. Luo, P. Testa, H. Gu, X.-Z. Chen, B. J. Nelson, L. J. Heyderman, Nanomagnetic encoding of shape-morphing micromachines. *Nature* **575**, 164–168 (2019).
6. S. Tottori, L. Zhang, F. Qiu, K. K. Krawczyk, A. Franco-Obregón, B. J. Nelson, Magnetic helical micromachines: Fabrication, controlled swimming, and cargo transport. *Adv. Mater.* **24**, 811–816 (2012).
7. O. Yasa, P. Erkoc, Y. Alapan, M. Sitti, Microalga-powered microswimmers toward active cargo delivery. *Adv. Mater.* **30**, 1804130 (2018).
8. Y. Alapan, O. Yasa, O. Schauer, J. Giltinan, A. F. Tabak, V. Sourjik, M. Sitti, Soft erythrocyte-based bacterial microswimmers for cargo delivery. *Sci. Robot.* **3**, eaar4423 (2018).
9. A. Aziz, M. Medina-Sánchez, J. Claussen, O. G. Schmidt, Real-time optoacoustic tracking of single moving micro-objects in deep phantom and ex vivo tissues. *Nano Lett.* **19**, 6612–6620 (2019).
10. X. Yan, Q. Zhou, M. Vincent, Y. Deng, J. Yu, J. Xu, T. Xu, T. Tang, L. Bian, Y.-X. J. Wang, K. Kostarelos, L. Zhang, Multifunctional biohybrid magnetite microrobots for imaging-guided therapy. *Sci. Robot.* **2**, eaaq1155 (2017).
11. B. J. Nelson, I. K. Kaliakatsos, J. J. Abbott, Microrobots for minimally invasive medicine. *Annu. Rev. Biomed. Eng.* **12**, 55–85 (2010).
12. H. Ceylan, I. C. Yasa, U. Kilic, W. Hu, M. Sitti, Translational prospects of untethered medical microrobots. *Prog. Biomed. Eng.* **1**, 012002 (2019).
13. J. C. Firrell, H. H. Lipowsky, Leukocyte margination and deformation in mesenteric venules of rat. *Am. J. Physiol. Heart Circ. Physiol.* **256**, H1667–H1674 (1989).

14. S. Kim, P. K. Ong, O. Yalcin, M. Intaglietta, P. C. Johnson, The cell-free layer in microvascular blood flow. *Biorheology* **46**, 181–189 (2009).
15. J. Weirather, S. Frantz, in *Inflammation in Heart Failure,* W. M. Blankesteijn, R. Altara, Eds. (Academic Press, 2015), chap. 2, pp. 19–38.
16. D. Ahmed, T. Baasch, N. Blondel, N. Läubli, J. Dual, B. J. Nelson, Neutrophil-inspired propulsion in a combined acoustic and magnetic field. *Nat. Commun.* **8**, 770 (2017).
17. S. Nourshargh, R. Alon, Leukocyte migration into inflamed tissues. *Immunity* **41**, 694–707 (2014).
18. N. R. Anderson, A. Buffone Jr., D. A. Hammer, T lymphocytes migrate upstream after completing the leukocyte adhesion cascade. *Cell Adh. Migr.* **13**, 164–169 (2019).
19. M. D. Savage, in *A Laboratory Guide to Biotin-Labeling in Biomolecule Analysis,* T. Meier, F. Fahrenholz, Eds. (Birkhäuser Basel, 1996), pp. 1–29.
20. U. Bozuyuk, O. Yasa, I. C. Yasa, H. Ceylan, S. Kizilel, M. Sitti, Light-triggered drug release from 3D-printed magnetic chitosan microswimmers. *ACS Nano* **12**, 9617–9625 (2018).
21. H.-S. Jung, D.-S. Moon, J.-K. Lee, Quantitative analysis and efficient surface modification of silica nanoparticles. *Journal of Nanomater.* **2012**, 93471 (2012).
22. B. Yigit, Y. Alapan, M. Sitti, Programmable collective behavior in dynamically self-assembled mobile microrobotic swarms. *Adv. Sci.* **6**, 1801837 (2019).
23. B. Yigit, Y. Alapan, M. Sitti, Cohesive self-organization of mobile microrobotic swarms. *Soft Matter* **16**, 1996 (2020).
24. A. Kaiser, A. Snezhko, I. S. Aranson, Flocking ferromagnetic colloids. *Sci. Adv.* **3**, e1601469 (2017).
25. M. H. Kroll, J. D. Hellums, L. McIntire, A. Schafer, J. Moake, Platelets and shear stress. *Blood* **88**, 1525–1541 (1996).
26. Y. Alapan, C. Kim, A. Adhikari, K. E. Gray, E. Gurkan-Cavusoglu, J. A. Little, U. A. Gurkan, Sickle cell disease biochip: A functional red blood cell adhesion assay for monitoring sickle cell disease. *Transl. Res.* **173**, 74–91.e8 (2016).
27. M. Kim, Y. Alapan, A. Adhikari, J. A. Little, U. A. Gurkan, Hypoxia-enhanced adhesion of red blood cells in microscale flow. *Microcirculation* **24**, e12374 (2017).
28. L. Soler, C. Martínez-Cisneros, A. Swiersy, S. Sánchez, O. G. Schmidt, Thermal activation of catalytic microjets in blood samples using microfluidic chips. *Lab Chip* **13**, 4299–4303 (2013).
29. S. Martel, J.-B. Mathieu, O. Felfoul, A. Chanu, E. Aboussouan, S. Tamaz, P. Pouponneau, L.'H. Yahia, G. Beaudoin, G. Soulez, M. Mankiewicz, Automatic navigation of an untethered device in the artery of a living animal using a conventional clinical magnetic resonance imaging system. *Appl. Phys. Lett.* **90**, 114105 (2007).
30. S. Jeong, H. Choi, G. Go, C. Lee, K. S. Lim, D. S. Sim, M. H. Jeong, S. Y. Ko, J. O. Park, S. Park, Penetration of an artificial arterial thromboembolism in a live animal using an intravascular therapeutic microrobot system. *Med. Eng. Phys.* **38**, 403–410 (2016).
31. S. Sanchez, A. A. Solovev, S. M. Harazim, O. G. Schmidt, Microbots swimming in the flowing streams of microfluidic channels. *J. Am. Chem. Soc.* **133**, 701–703 (2011).
32. R. D. Field, P. N. Anandakumaran, S. K. Sia, Soft medical microrobots: Design components and system integration. *Appl. Phys. Rev.* **6**, 041305 (2019).
33. J. J. Abbott, Z. Nagy, F. Beyeler, B. J. Nelson, Robotics in the small, part I: Microbotics. *IEEE Robot. Autom. Mag.* **14**, 92–103 (2007).
34. Y. Alapan, Y. Matsuyama, J. Little, U. Gurkan, Dynamic deformability of sickle red blood cells in microphysiological flow. *Technology* **4**, 71–79 (2016).
35. Y. Alapan, A. Fraiwan, E. Kucukal, M. N. Hasan, R. Ung, M. Kim, I. Odame, J. A. Little, U. A. Gurkan, Emerging point-of-care technologies for sickle cell disease screening and monitoring. *Expert Rev. Med. Devices* **13**, 1073–1093 (2016).
36. D. Disharoon, K. B. Neeves, D. W. M. Marr, ac/dc magnetic fields for enhanced translation of colloidal microwheels. *Langmuir* **35**, 3455–3460 (2019).
37. A. C. Hortelão, R. Carrascosa, N. Murillo-Cremaes, T. Patiño, S. Sánchez, Targeting 3D bladder cancer spheroids with urease-powered nanomotors. *ACS Nano* **13**, 429–439 (2019).
38. F. Chen, H. Hong, Y. Zhang, H. F. Valdovinos, S. Shi, G. S. Kwon, C. P. Theuer, T. E. Barnhart, W. Cai, In vivo tumor targeting and image-guided drug delivery with antibody-conjugated, radiolabeled mesoporous silica nanoparticles. *ACS Nano* **7**, 9027–9039 (2013).
39. M. Karimi, A. Ghasemi, P. Sahandi Zangabad, R. Rahighi, S. M. Moosavi Basri, H. Mirshekari, M. Amiri, Z. Shafaei Pishabad, A. Aslani, M. Bozorgomid, D. Ghosh, A. Beyzavi, A. Vaseghi, A. R. Aref, L. Haghani, S. Bahrami, M. R. Hamblin, Smart micro/nanoparticles in stimulus-responsive drug/gene delivery systems. *Chem. Soc. Rev.* **45**, 1457–1501 (2016).
40. C. S. Linsley, B. M. Wu, Recent advances in light-responsive on-demand drug-delivery systems. *Ther. Deliv.* **8**, 89–107 (2017).
41. A. Barhoumi, Q. Liu, D. S. Kohane, Ultraviolet light-mediated drug delivery: Principles, applications, and challenges. *J. Control. Release* **219**, 31–42 (2015).
42. S. Liu, M. Han, Synthesis, functionalization, and bioconjugation of monodisperse, Silica-Coated gold nanoparticles: Robust bioprobes. *Advanced Functional Materials* **15**, 961–967 (2005).
43. V. Hong, S. I. Presolski, C. Ma, M. Finn, Analysis and optimization of copper-catalyzed azide–alkyne cycloaddition for bioconjugation. *Angew. Chem. Int. Ed.* **48**, 9879–9883 (2009).
44. Y. Alapan, K. Icoz, U. A. Gurkan, Micro-and nanodevices integrated with biomolecular probes. *Biotechnol. Adv.* **33**, 1727–1743 (2015).
45. Y. Alapan, J. A. Little, U. A. Gurkan, Heterogeneous red blood cell adhesion and deformability in sickle cell disease. *Sci. Rep.* **4**, 7173 (2014).
46. A. J. Goldman, R. G. Cox, H. Brenner, Slow viscous motion of a sphere parallel to a plane wall—I Motion through a quiescent fluid. *Chem. Eng. Sci.* **22**, 637–651 (1967).
47. T.-Y. Chiang, D. Velegol, Localized electroosmosis (LEO) induced by spherical colloidal motors. *Langmuir* **30**, 2600–2607 (2014).
48. T. Li, A. Zhang, G. Shao, M. Wei, B. Guo, G. Zhang, L. Li, W. Wang, Janus microdimer surface walkers propelled by oscillating magnetic fields. *Adv. Funct. Mater.* **28**, 1706066 (2018).

Acknowledgments: Y.A. thanks the Alexander von Humboldt Foundation for the Humboldt Postdoctoral Research Fellowship. We thank B. H. Domac for helping with the preliminary experiments, D. Sheehan and K. Richardson for cell culture and biological experiments, A. Aghakhani and B. Yigit for discussions, M. Birgul Akolpoglu for SEM analysis, and J. Giltinan for helping with the magnetic actuation setup. **Funding:** This work is funded by the Max Planck Society. **Author contributions:** U.B. and Y.A. participated in the study design, experimental procedures, data collection, data analysis, and manuscript writing. P.E. participated in the study design and assisted with experimental procedures. A.C.K. assisted with experimental procedures. M.S. participated in the study design and manuscript writing. **Competing interests:** The authors declare that they have no competing financial interests. **Data and materials availability:** All data needed to evaluate the conclusions in the paper are present in the paper or the Supplementary Materials. Contact M.S. for materials.

Submitted 14 December 2019
Accepted 3 April 2020
Published 20 May 2020
10.1126/scirobotics.aba5726

Citation: Y. Alapan, U. Bozuyuk, P. Erkoc, A. C. Karacakol, M. Sitti, Multifunctional surface microrollers for targeted cargo delivery in physiological blood flow. *Sci. Robot.* **5**, eaba5726 (2020).

Science Robotics

Multifunctional surface microrollers for targeted cargo delivery in physiological blood flow

Yunus Alapan, Ugur Bozuyuk, Pelin Erkoc, Alp Can Karacakol, and Metin Sitti

Sci. Robot. **5** (42), eaba5726. DOI: 10.1126/scirobotics.aba5726

Science Robotics (ISSN 2470-9476) is published by the American Association for the Advancement of Science. 1200 New York Avenue NW, Washington, DC 20005. The title *Science Robotics* is a registered trademark of AAAS.